

Three-dimensional heat and material flow during friction stir welding of mild steel

R. Nandan ^{a,*}, G.G. Roy ^a, T.J. Lienert ^b, T. Debroy ^a

^a Department of Materials Science and Engineering, The Pennsylvania State University, University Park, PA 16802, USA

^b Materials Science and Technology, Los Alamos National Laboratory, Los Alamos, NM, USA

Received 15 April 2006; received in revised form 3 September 2006; accepted 7 September 2006

Available online 4 December 2006

Abstract

Three-dimensional viscoplastic flow and heat transfer during friction stir welding of mild steel were investigated both experimentally and theoretically. The equations of conservation of mass, momentum and energy were solved in three dimensions using spatially variable thermo-physical properties and a methodology adapted from well-established previous work in fusion welding. Non-Newtonian viscosity for the metal flow was calculated considering temperature and strain rate dependent flow stress. The computed results showed significant viscoplastic flow near the tool surface, and convection was found to be the primary mechanism of heat transfer in this region. Also, the results demonstrated the strong three-dimensional nature of the transport of heat and mass, reaffirming the need for three-dimensional calculations. The streamlines of plastic flow indicated that material was transported mainly along the retreating side. The computed temperatures were in good agreement with the corresponding experimentally determined values.

© 2006 Published by Elsevier Ltd on behalf of Acta Materialia Inc.

Keywords: Friction stir welding; Numerical modeling; Mild steel; Plastic flow; Heat transfer

1. Introduction

Friction stir welding (FSW) is a solid-state welding process. The tool usually has a large-diameter shoulder and a smaller threaded pin. The plates to be welded are aligned together and clamped using fixtures. A cylindrical hole is drilled at one end of the workpiece on the centerline and the pin is inserted into the hole, with the shoulder in contact with the top surface of the workpiece. The tool is rotated at high speed as it is moved along the weld centerline. Heat is generated by friction between the tool and the workpiece and by the plastic deformation of the workpiece material. A schematic diagram of the FSW system is shown in Fig. 1. The heat transfer and plastic flow depend on material properties as well as welding variables like the rotational and translational speeds of the tool and the tool design. The complex interactions between the various

simultaneously occurring physical processes affect the heating and cooling rates and the structure and properties of the welded joints.

The FSW process was discovered in 1991 at TWI [1]. Since then FSW has been widely studied both experimentally and theoretically to better understand both the welding process and the welded materials. Most of the early quantitative studies were based on heat conduction and ignored the plastic flow near the tool [2,3]. Several heat generation models were proposed to quantitatively describe the frictional heat generation at the interface between the tool and the workpiece and the internal heat generation within the workpiece due to plastic deformation [4,5]. Several researchers [6,7] investigated the partitioning of heat between the tool and the workpiece for the FSW of different engineering alloys. Khandkar et al. [8] developed a three-dimensional thermal model where the heat generation was modeled based on experimentally measured torque distribution. They adjusted the bottom heat transfer coefficient to achieve good agreement between the com-

* Corresponding author.

E-mail address: rituraj@psu.edu (R. Nandan).

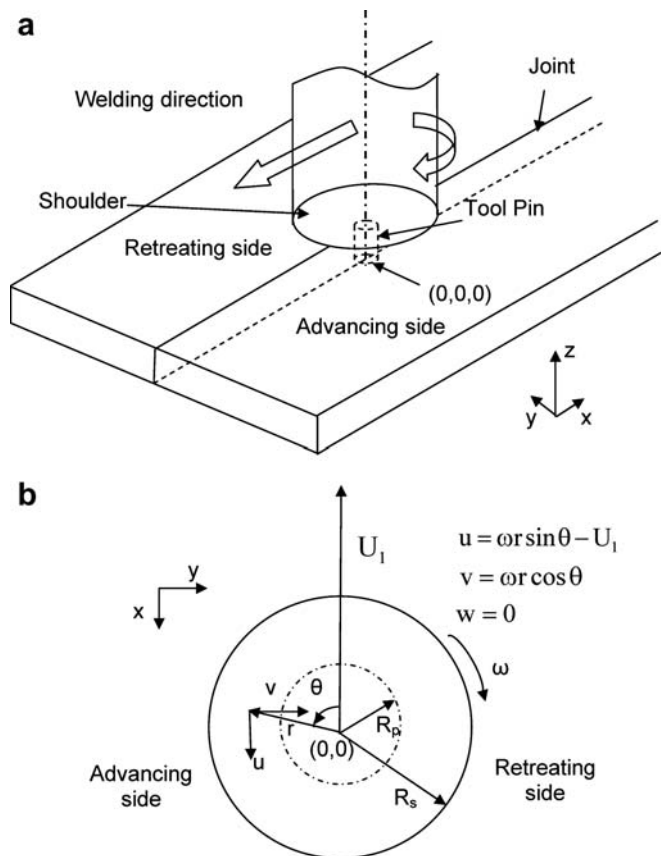


Fig. 1. A schematic diagram of the FSW system considered in the model showing the thermal boundary conditions. (b) Top view of the tool showing tool velocity at the tool shoulder work piece interface. $\theta = 0$ corresponds to plane $x < 0$.

puted and the measured temperatures. Although the heat conduction models provided important insight about the FSW process, these initial models ignored convective heat transfer due to viscoplastic flow of metals.

Work on the development of rigorous models of heat transfer in FSW considering materials flow is just beginning. Seidel and Reynolds [9] developed a two-dimensional thermal model based on laminar, viscous and non-Newtonian flow around a circular cylinder. They observed that significant vertical mixing occurred during FSW, particularly at low values of welding speed to rotational speed ratios. This fact indicates the need for three-dimensional models. Colegrove and Shercliff [10,11] used a commercial CFD software, FLUENT, to develop a three-dimensional heat and material flow model during friction stir welding of 7075 Al alloy. They used the thermal and materials flow model to investigate tool design. Interestingly, the different tool designs did not result in any significant changes in either the heat input or the power requirement. In another study [12] they examined the effect of tool orientation on the traversing force.

Smith et al. [13] experimentally determined viscosity as a function of shear rate and temperature for the AA 6061-T6 alloy, which was then incorporated into a three-dimensional coupled heat and material flow model for the FSW of 6061

aluminum alloy. Ulysse [14] modeled the effects of tool speeds, both rotational and linear, on forces and plate temperatures during FSW of thick aluminum plates, based on a three-dimensional viscoplastic model. Most recently, Nandan et al. reported results of a three-dimensional material flow and heat transfer model during FSW of 6061 aluminum alloy [15] and 304 austenitic stainless steel [16]. They calculated the temperature fields, cooling rates, plastic flow fields and the geometry of the thermomechanically affected zone (TMAZ) using spatially variable heat generation rates, non-Newtonian viscosity as a function of local strain rate and temperature, and temperature-dependent thermal conductivity, specific heat and yield stress. The computed temperature fields and TMAZ agreed well with the corresponding independent experimental data.

Although several numerical models of FSW of aluminum alloy have been reported in the literature, most of these were not concerned with the FSW of steel. There are a few exceptions. Zhu and Chao [17] proposed a three-dimensional thermal model without considering plastic flow for 304L stainless steel. Two-dimensional steady-state heat transfer and fluid flow near the tool pin was modeled by Cho et al. [18] for the FSW of 304L stainless steel. They used a simplified Hart's model [19] to calculate the flow stress and non-Newtonian viscosity. Isotropic strain hardening was included in the finite element solution procedure. The workpiece temperatures were computed assuming various tool temperatures and heat transfer coefficients. They found that higher tool temperatures and heat transfer coefficients resulted in higher workpiece temperatures. The experimental and the computed results indicated that the temperatures were about 100 K higher on the advancing side than on the retreating side.

Here we present a detailed numerical analysis of three-dimensional material flow and heat transfer during FSW of mild steel. In particular, we examine the temperature fields, cooling rates and plastic flow fields by solving the equations of conservation of mass, momentum and energy in three dimensions with appropriate boundary conditions.

Table 1
Data used in the calculations

Property/weld parameter	Value
Workpiece length (x-direction)	0.41 m
Workpiece half-width (y-direction)	0.078 m
Workpiece thickness	6.35 mm
Shoulder radius	9.5 mm
Pin radius	3.95 mm
Pin length	6.22 mm
Weld speed	0.42 mm/s
Rotational speed	450 rpm
Workpiece material	Mild steel
Density	7860 kg/m ³
Axial pressure [20], P_T	65.9 MPa
Coefficient of friction, μ	0.41–0.28
Percentage slip, δ	0–0.8
Heat transfer coefficient from bottom	50 W/m ² K
Tool material	Tungsten
Density	19,400 kg/m ³

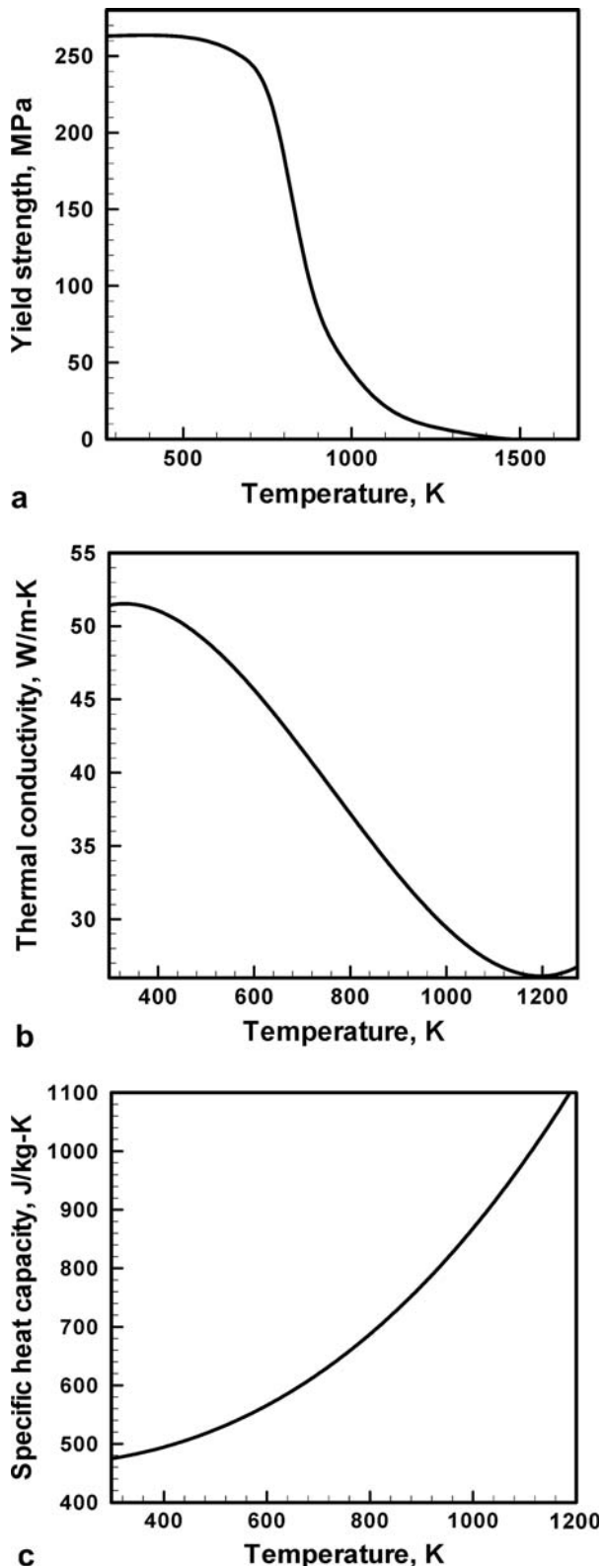


Fig. 2. Variations of (a) yield strength, (b) thermal conductivity and (c) specific heat capacity of mild steel with temperature [26]. The curves are obtained by spline interpolation of the data points obtained from literature.

The computed values of strain rates, viscosity, velocities and temperatures during FSW of steel are compared with the corresponding values typically obtained during the

FSW of aluminum alloys. The nature of materials flow around the pin is understood through the examination of streamlines. The model considers spatially variable heat generation rates, non-Newtonian viscosity as a function of local strain rate, temperature and the nature of the material, and temperature-dependent thermal conductivity, specific heat and yield stress. Numerically computed temperature fields and the total torque on the tool were compared with the corresponding experimentally measured values.

2. Materials and experiments

Friction stir welding of hot rolled AISI 1018 steel was conducted in square groove butt joint configuration with a tungsten tool. The plates were 203 mm in length, 101 mm in width and 6.35 mm in thickness. The tool had a shoulder of 19 mm and a cylindrical pin of 6.22 mm length and 7.9 mm diameter [20]. The cylindrical pin was threaded with a pitch of 1 mm. Thus, the length of the pin was slightly smaller than the workpiece thickness. The 1018 Mn-steel used in the experiments contained 0.18% C, 0.82% Mn, 0.011% P, 0.006% S and less than 0.01% Si. The thermo-physical properties of the steel and the tool material are given in Table 1 and Fig. 2.

3. Mathematical modeling

3.1. Assumptions

Except at the beginning and end of welding, heat is generated at a constant rate during the intermediate period and the cross-sections of the welds demonstrate similar geometry, structure and properties, indicating a quasi-steady behavior [21]. Shortly after the start of welding, the cylindrical tool shoulder and the tool pin rotate at a constant speed, with the tool pin completely inserted within the workpiece. The mass flow is treated as a flow of a non-Newtonian, incompressible, viscoplastic material. The maximum shear stress for yielding was assumed to be $\tau = \sigma_{\text{yield}}/\sqrt{3}$ where the yield stress, σ_{yield} , is based on distortion energy theory for plane stress. The density variation was ignored following Boussinesq's approximation. Partial sticking condition was assumed at the surface between the tool and the workpiece. The tilt angle of the tool is taken as zero. Also, the tool shoulder is assumed to be flat.

Fixed non-uniform grids with coordinates attached to the moving tool axis were used. The origin of the coordinates and the directions are indicated in Fig. 1a. As indicated in Fig. 1b, angle θ is the angle with the negative x -axis in the counter-clockwise direction ($\theta = 0^\circ$ corresponds to plane $x < 0$).

3.2. The governing equations

The continuity equation for incompressible single-phase flow in index notation for $i = 1, 2$ and 3, representing the x , y and z directions, respectively is given by

$$\frac{\partial u_i}{\partial x_i} = 0 \quad (1)$$

where u is the velocity of plastic flow. The steady single phase momentum conservation equations with reference to a coordinate system attached to the heat source in index form may be represented as [22]:

$$\rho \frac{\partial u_i u_j}{\partial x_i} = -\frac{\partial p}{\partial x_j} + \frac{\partial}{\partial x_i} \left(\mu \frac{\partial u_j}{\partial x_i} + \mu \frac{\partial u_i}{\partial x_j} \right) - \rho U_1 \frac{\partial u_j}{\partial x_1} \quad (2)$$

where ρ is the density, μ is the non-Newtonian viscosity, U_1 is the welding velocity and p is the pressure. The constitutive equations used here for viscosity calculation have been used for hot-working processes, particularly extrusion. Friction stir welding involves transfer of plasticized material from the front to the back of the tool pin as the tool traverses along the joint. It is basically an extrusion process followed by forging which joins the plates. Therefore, it is appropriate to use these equations for FSW. The calculation of viscosity requires local values of strain rate and temperature. The viscosity was calculated based on the following formulation of flow stress, σ_e , proposed by Sheppard and Wright [23]:

$$\sigma_e = \frac{1}{\alpha} \sinh^{-1} \left[\left(\frac{Z}{A} \right)^{1/n} \right] \quad (3)$$

where A , α and n are material constants and Z is the Zener–Hollomon parameter. Parameter A is a function of the carbon concentration in C–Mn-steel, while α and n depend on the temperature, T , as indicated below [24]:

$$A = 1.80 \times 10^6 + 1.74 \times 10^8 (\%C) - 6.5 \times 10^7 (\%C)^2 \quad (4)$$

$$\alpha = 1.07 + 1.70 \times 10^{-4} T - 2.81 \times 10^{-7} T^2 \quad (5)$$

$$n = 0.2 + 3.966 \times 10^{-4} T \quad (6)$$

Z , the Zener–Hollomon parameter, represents the temperature compensated effective strain rate and is given by

$$Z = \dot{\epsilon} \exp \left(\frac{Q}{RT} \right) \quad (7)$$

Here Q is the temperature independent activation energy, R is gas constant and $\dot{\epsilon}$ is the effective strain rate, given by

$$\dot{\epsilon} = \left(\frac{2}{3} \varepsilon_{ij} \varepsilon_{ij} \right)^{1/2} \quad (8)$$

where ε_{ij} is the strain rate tensor, defined as

$$\varepsilon_{ij} = \frac{1}{2} \left(\frac{\partial u_i}{\partial x_j} + \frac{\partial u_j}{\partial x_i} \right) \quad (9)$$

Finally, viscosity can be determined from flow stress and effective strain rate using Perzyna's viscoplasticity model [25]

$$\mu = \frac{\sigma_e}{3\dot{\epsilon}} \quad (10)$$

The above formulation indicates that dynamic viscosity is a strong function of local strain rate and temperature.

Fig. 3 shows the computed variation of viscosity, expressed as a logarithm to the base of 10, with strain rate and temperature. The results show that viscosity decreases significantly with both strain rate and temperature. The strain rate is the more dominant factor for the conditions typical of FSW. For the same temperature and strain rate, the viscosity values are about one order of magnitude higher than those reported for the FSW of aluminum [15].

The steady thermal energy conservation equation is given by

$$\rho C_p \frac{\partial (u_i T)}{\partial x_i} = -\rho C_p U_1 \frac{\partial T}{\partial x_1} + \frac{\partial}{\partial x_i} \left(k \frac{\partial T}{\partial x_i} \right) + S_i + S_b \quad (11)$$

where C_p is the specific heat and k is the thermal conductivity of the workpiece/tool. The term S_i represents the source term due to interfacial heat generation rate per unit volume at the tool pin–workpiece interface and S_b is the heat generation rate due to plastic deformation in the workpiece away from the interface. The heat generated at the interface between vertical and horizontal surface of the tool pin and the workpiece, S_i , may be defined as:

$$S_i = [(1 - \delta)\eta\tau + \delta\mu_f P_N] (\omega r - U_1 \sin \theta) \frac{A_r}{V} \quad (12)$$

where A_r is any small area on the tool pin–workpiece interface, r is the radial distance of the center of the area from the tool axis, V is the control-volume enclosing the area A_r , τ is the maximum shear stress at yielding, θ is the angle with the negative x -axis in the counter-clockwise direction, η is the mechanical efficiency, i.e. the amount of mechanical energy converted to heat energy, δ denotes the spatially variable fractional slip between the tool and the workpiece interface, μ_f is the spatially variable coefficient of friction, ω is the angular velocity and P_N is the normal pressure

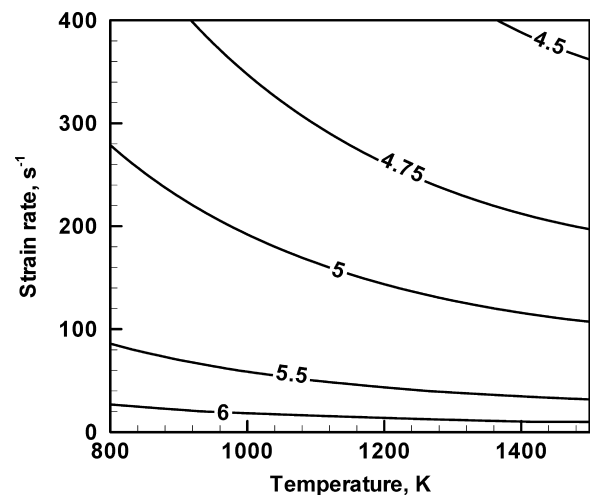


Fig. 3. Computed contours of viscosity as a function of temperature and strain rate. The contour labels represent logarithm to the base 10 of viscosity in Pa s.

on the surface, which is equal to P_V for the workpiece area in contact with the vertical surface of the pin and equal to P_H for area below the horizontal surface of the tool. The velocity $(\omega r - U_1 \sin \theta)$ represents the local velocity of a point on tool with the origin fixed at the tool axis.

A 50% mechanical efficiency was assumed guided by the range of the previous work in FSW [6,17]. In Eq. (12) the radial pressure is much smaller than the axial pressure and the value of P_V has been assumed to be zero. When δ is 0, full sticking is indicated and all the heat is generated by plastic deformation, while heat is generated only by friction when $\delta = 1$. The variation of yield stress for mild steel alloy with temperature is shown in Fig. 2(a) based on data available in Ref. [26].

During FSW, mixing is not atomic, as evident from the previous research on dissimilar metal joining [27]. Here grains are deformed but efficient mixing of atoms does not occur. A rigorous calculation of heat generation due to viscous dissipation of momentum is difficult. However, previous research has shown that the heat generation due to viscous dissipation is small, of the order of only 4.4% of the total heat generation for the FSW of aluminum alloy [28]. A rough estimate of the viscous dissipation of momentum per unit volume, S_b , has been calculated as $f_m \mu \Phi$, where Φ is given by [27,28]:

$$\Phi = 2 \left(\left(\frac{\partial u_1}{\partial x_1} \right)^2 + \left(\frac{\partial u_2}{\partial x_2} \right)^2 + \left(\frac{\partial u_3}{\partial x_3} \right)^2 \right) + \left(\frac{\partial u_1}{\partial x_2} + \frac{\partial u_2}{\partial x_1} \right)^2 + \left(\frac{\partial u_1}{\partial x_3} + \frac{\partial u_3}{\partial x_1} \right)^2 + \left(\frac{\partial u_3}{\partial x_2} + \frac{\partial u_2}{\partial x_3} \right)^2 \quad (13)$$

and f_m is an arbitrary constant that indicates the extent of atomic mixing in the system. The value of f_m will tend to 1 for a well-mixed system in the atomic scale. In systems where the grains remain largely intact, the value of f_m will be very small. Here, a value of 0.05 was used because this value resulted in the viscous dissipation being about 4% of the total heat generation for the welding conditions investigated. The viscous dissipation term is particularly important because, without this term, the temperature field calculated from Eq. (11) does not change significantly with change in viscosity.

3.3. Boundary conditions

Since the thermal conductivity of the tool material (tungsten) is around four times higher than steel, a significant amount of heat will be transported to the tool material. Therefore, the total heat generated at the shoulder–workpiece interface has been partitioned between the workpiece and the tool in the ratio given below:

$$f = \frac{J_W}{J_T} = \frac{\sqrt{(k\rho C_p)_W}}{\sqrt{(k\rho C_p)_T}} \quad (14)$$

where the subscripts W and T denote the workpiece and the tool, respectively. The analytical expression is based on steady-state one-dimensional heat transfer from a point heat source located at the interface of dissimilar metals [29]. Based on the data in Table 1 and Fig. 2 at 1000 K, the estimated heat flux into the workpiece is calculated as 43%. This relation has been examined experimentally by Lienert et al. [20] and found to be reliable.

A heat flux continuity at the shoulder–matrix interface yields:

$$k \frac{\partial T}{\partial z} \Big|_{\text{top}} = \frac{J_W}{J_W + J_T} q_1 \text{ in the range } R_P \leq r \leq R_S \quad (15)$$

R_P and R_S represent the tool pin and shoulder radius, respectively, and q_1 represents the rate of heat generation due to plastic work at the shoulder–workpiece interface. It is given by

$$q_1 = [(1 - \delta)\eta\tau + \delta\mu_t P_T](\omega r - U_1 \sin \theta) \quad (16)$$

The boundary condition for heat exchange between the top surface of the workpiece and the surroundings beyond the shoulder involved consideration of both convective and radiative heat transfer as

$$-k \frac{\partial T}{\partial z} \Big|_{\text{top}} = \sigma\varepsilon(T^4 - T_a^4) + h_t(T - T_a) \quad (17)$$

At the bottom surface, the heat transfer coefficient based on the previously reported value [18] was used:

$$k \frac{\partial T}{\partial z} \Big|_{\text{bottom}} = h_b(T - T_a) \quad (18)$$

Velocity at the tool pin periphery have been defined in terms of tool translation velocity and the tool pin angular velocity

$$\begin{aligned} u &= (1 - \delta)(\omega R_P \sin \theta - U_1) \\ v &= (1 - \delta)\omega R_P \cos \theta \\ w &= \kappa \frac{\omega}{2\pi} R_P \end{aligned} \quad (19)$$

where κ denotes the pitch of the threads on the cylindrical tool.

Similarly, at the shoulder contact, the velocity condition may be written as:

$$\left. \begin{aligned} u &= (1 - \delta)(\omega r \sin \theta - U_1) \\ v &= (1 - \delta)\omega r \cos \theta \end{aligned} \right\} \text{ in the range } R_P \leq r \leq R_S \quad (20)$$

At all other surfaces, temperatures are set to ambient temperature and the velocities are set to zero.

The governing equations and the boundary conditions were implemented in a computer code. The solution procedure based on the SIMPLE algorithm [30], capable of calculating three-dimensional heat transfer and fluid flow with a stationary or moving heat source, with a free or flat surface, has been well tested and has been recently reported for the calculations of heat transfer and fluid flow in several

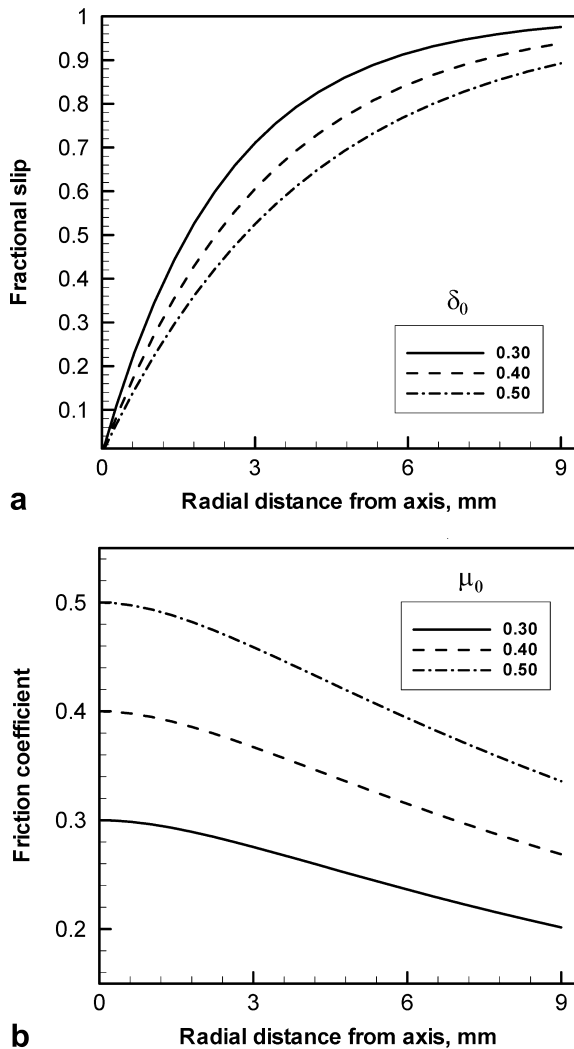


Fig. 4. Variations of (a) fractional slip (δ) and (b) friction coefficient (μ_f) with radial distance from the tool axis for different scaling constants. For (b), δ_0 was fixed at 0.40. Rotational speed was 450 rpm.

welding processes [22,31–37]. The data used for the calculations are presented in Table 1.

The extent of slip was estimated from the following functional relationship determined from the reported experimental data of tool–workpiece interfacial slip in a flat-wedge cross-wedge rolling process [38]. The trend of the reported data can be expressed by the following relation for FSW:

$$\delta = 1 - \exp\left(-\frac{1}{\delta_0} \frac{\omega}{\omega_0} \frac{r}{R_S}\right) \quad (21)$$

where δ denotes the fraction-slip and δ_0 is a constant. Fig. 4a shows the variation of slip with radial distance. The above equation was used for all interfaces, with r denoting the distance of the center of the area from the tool axis. It is constant at R_P for the vertical surface of the pin, varies from 0 to R_P for the horizontal surface and varies from R_P to R_S for the tool shoulder. The value of δ_0 was taken as 0.4. This value resulted in good agreement be-

tween computed and experimental temperature values. A typical value of rotational speed, ω_0 , was used to non-dimensionalize the tool rotational speed of the tool, ω , and R_S is the shoulder radius.

Values of friction coefficient were calculated considering the relative velocity between the tool and the workpiece guided by previous work in the field of friction welding of steel bars [39,40]. The relative velocity increases from zero at the axis of rotation (static condition) to ωR_S at the periphery of the tool shoulder (dynamic condition). Experimental evidence in Refs. [38,39] suggest that μ has the following form:

$$\mu_f = \mu_0 \exp(-\lambda \delta \omega r) \quad (22)$$

where δ is the percentage sticking and r is the radial distance from the tool axis for the point in consideration. The value of μ_0 was taken as 0.4 and constant λ was 1 s/m. Fig. 4b shows the variation of friction coefficient with radial distance from the tool axis.

4. Results and discussion

4.1. Heat generation rates

The proportion of the heat generated at the tool shoulder and the pin surfaces is determined by the tool geometry and the welding variables. For the experimental conditions studied in this work, the computed heat generation rates, peak temperatures and the total torque on the tool are presented in Table 2. Fig. 5 shows the spatial variation of heat generation pattern at the tool–workpiece interfaces. Fig. 5a shows that the heat generation pattern at the tool shoulder is nearly symmetric about the tool axis. The relative velocity between the workpiece and the shoulder increases with distance from the axis. As a result, more heat is generated further away from the axis near the shoulder. The heat generation rate at the bottom of the pin shown in Fig. 5b indicates a similar behavior. The angular variation of heat generation rate on the tool surface is shown in Fig. 5c. The non-uniformity in the heat generation pattern results from the difference in the relative velocity at different angular locations on the pin surface, which arises due to the variation in term $U_1 \sin \theta$. However, the local differences in heat generation rates do not lead to significant variations of local temperatures because of the rapid recirculation of a layer of plasticized material near the pin surface. The flow pattern of the plasticized material and its role in heat transfer will be discussed later in the paper.

4.2. Computed temperature fields

The computed temperature profiles along the longitudinal and transverse sections through the tool axis and at the top surface of the workpiece are shown in Fig. 6a–c, respectively. The temperature profiles on the longitudinal mid-section (Fig. 6a) and on the top surface of the workpiece

Table 2
Heat generated at different locations, peak temperature and total torque on the tool for different welding parameters

Weld speed (mm/s)	Rotational speed (rpm)	Heat from shoulder (W)	Heat from tool pin's vertical surface (W)	Heat from tool pin's bottom (W)	Heat due to viscous dissipation (W)	Peak temperature (K)	Torque (N m)
0.02	350	608.7	272.7	135.4	54.1	1170.0	68.8
0.06	350	616.0	288.3	141.5	143.9	1137.6	70.9
0.10	350	620.3	304.1	147.6	166.5	1106.9	72.6
0.14	350	630.4	325.6	154.8	187.4	1061.0	75.5
0.02	450	694.8	247.7	162.2	25.5	1229.2	55.2
0.06	450	706.2	276.0	172.5	91.6	1168.0	58.0
0.10	450	709.8	290.2	178.6	129.3	1140.1	59.2
0.14	450	716.6	310.3	186.0	154.7	1097.2	61.1
0.02	550	763.0	211.7	185.8	16.8	1292.7	45.6
0.06	550	775.5	248.7	199.5	41.4	1210.5	48.4
0.10	550	780.9	267.6	207.4	99.5	1170.0	49.8
0.14	550	785.6	285.4	214.6	123.3	1128.3	51.0
0.02	650	819.8	176.5	207.9	13.3	1350.6	38.9
0.06	650	831.2	216.2	223.6	21.4	1253.9	41.3
0.10	650	837.8	241.4	234.0	81.5	1193.2	42.8
0.14	650	841.0	256.2	240.6	99.6	1152.3	43.7

(Fig. 6c) are compressed in front of the tool and expanded behind it. The computed results are consistent with the fact that heat is supplied rapidly to the cold region of the workpiece ahead of the tool while heat is transported at a slower rate to material already preheated behind the tool. This asymmetry results from the motion of the tool and becomes more prominent at high welding speeds. However, no significant asymmetry could be observed from Fig. 6b due to angular variation of heat generation and material flow. This behavior may be attributed to the smaller size of the tool considered in the present study. Fig. 7 depicts the computed thermal cycles at several monitoring locations. The locations are 2 mm below the top surface of the workpiece and at 4, 8 and 12 mm from the welding direction in the retreating side. Thermal cycles were constructed from the steady state temperature distribution by converting distance traveled by tool pin to time using welding velocity [36]. The results show a rapid increase in temperature during heating followed by a comparatively slower cooling as the heat source moves away from the monitoring locations. This behavior may be further explained from the temperature contours similar to those in Fig. 6c. The initial rapid heating is observed as the monitoring locations encounter compressed thermal contours ahead of the tool. As the tool moves ahead of the monitoring locations, the expanded temperature contours lead to slow cooling. The higher the welding velocity, the faster the temperature changes during both heating and cooling.

The computed thermal cycle at a distance of 12.7 mm from axis of the tool on the advancing side is compared with the experimental data in Fig. 8. Good agreement between the experimentally determined and the computed results indicates that the model can be used to predict temperature profiles and cooling rates.

Fig. 9a shows the variation of the computed peak temperature in the workpiece with friction coefficient for different extents of slip. Since no specified extent of slip has been reported in the literature, the sensitivity of the peak temperature on the extent of slip was examined. It is observed that peak temperature increases with higher slip. This trend is consistent with higher heat generation due to friction than shearing at the interface between the tool and the workpiece for the conditions typical of FSW of the mild steel. Fig. 9b shows that peak temperature increases with mechanical efficiency. As expected, the peak temperature is sensitive to mechanical efficiency.

4.3. The computed viscosity and plastic flow fields

Fig. 10 shows the computed strain rate vs. distance behind the tool opposite to the direction of welding at different elevations, i.e. values of z . The figure shows that maximum strain rate occurs near the surface of the pin where the maximum velocity gradient is present. For lower planes, strain rate rapidly decreases with distance away from the tool axis. For higher planes, close to the shoulder, the velocity gradient decreases gradually away from the

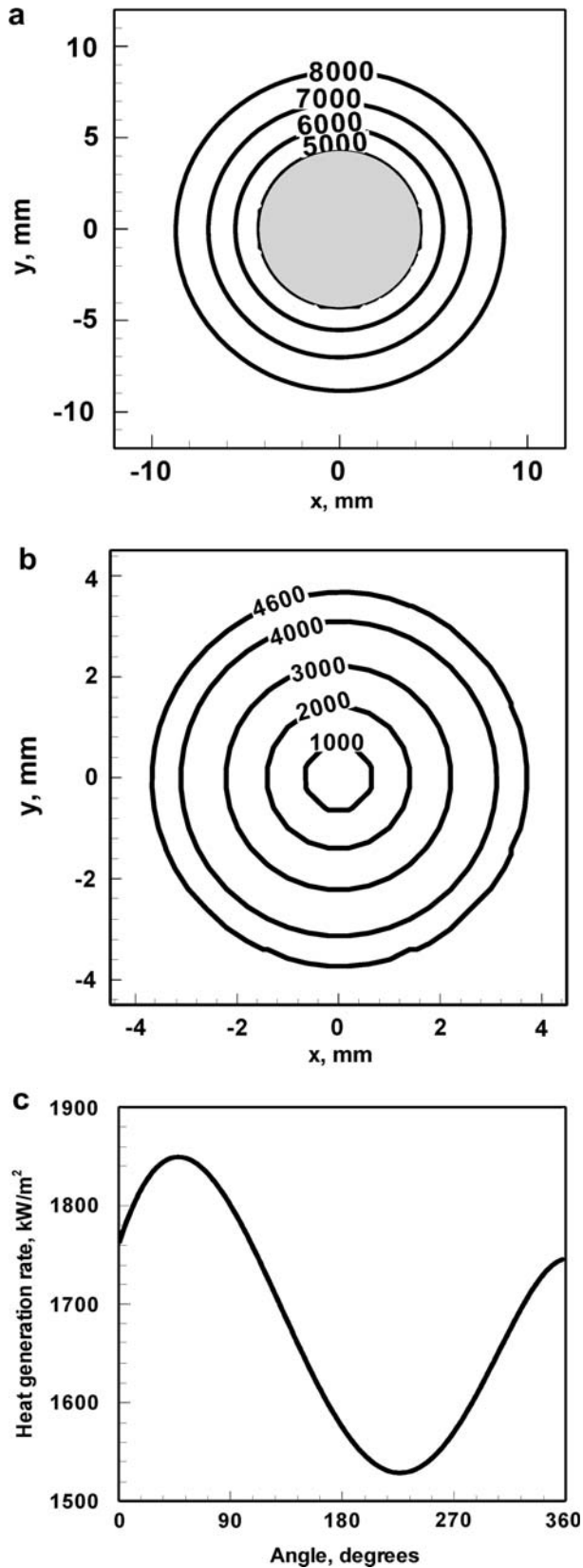


Fig. 5. Spatially variable heat generation rate at (a) the tool shoulder, (b) the bottom of the tool pin, and (contour values are in kW/m²) (c) the curved surface of the tool pin. The welding velocity was 0.42 mm/s and the rotational speed was 450 rpm.

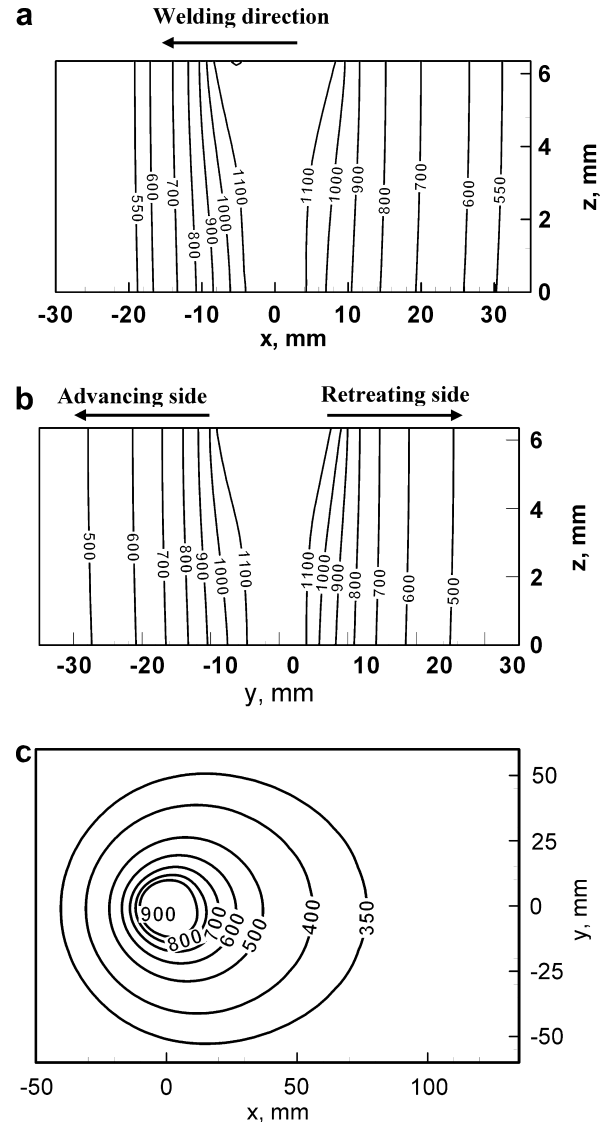


Fig. 6. Computed temperature profiles (K) in (a) $y = 0$ (xz -plane), (b) $x = 0$ (yz -plane) and (c) $z = 6.35$ mm (xy -plane), i.e. the top surface of the workpiece. The welding velocity was 0.42 mm/s and the rotational speed was 450 rpm.

tool axis to below the shoulder periphery. Beyond the periphery, the velocity gradient decreases sharply because of the rapid decay of velocity. The maximum value of strain rate achieved was 40 s^{-1} . It is also observed that strain rates decreases rapidly with depth, which may be attributed to large decrease in velocities away from the shoulder through viscous dissipation.

Fig. 11 shows the variation of viscosity along the x -direction at different elevations, i.e. values of z . It is seen that, at $z = 5.72$ mm, viscosity decreases with increasing x followed by a sharp increase at high values of x . Since the viscosity is inversely proportional to local strain rate, this observation may be explained considering the values of strain rates presented in Fig. 10, where the strain rate trends are just opposite to those of the viscosity values presented in Fig. 11. At lower values of z , the viscosity pro-

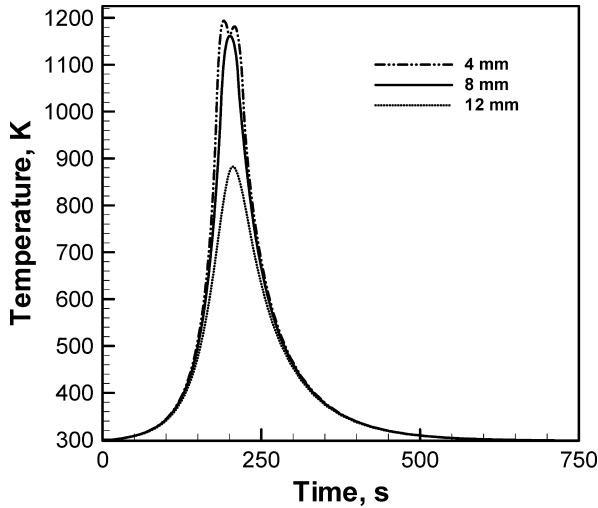


Fig. 7. Time-temperature profiles at several monitoring locations 3 mm below the top surface and at distances of 4, 8 and 12 mm from the centerline perpendicular to the welding direction in the advancing side. The welding velocity was 0.42 mm/s and the rotational speed was 450 rpm.

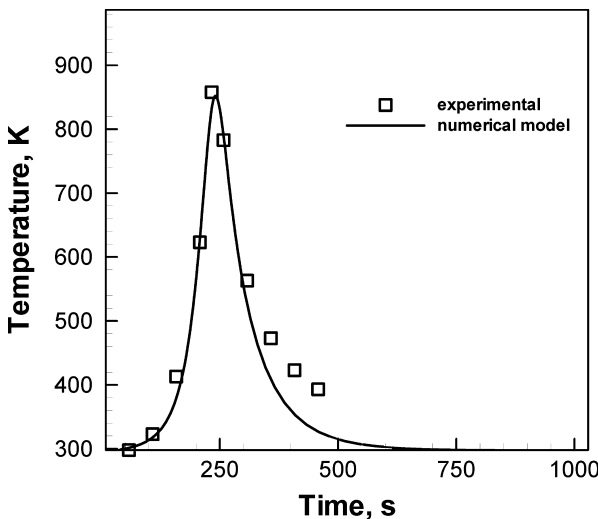


Fig. 8. Comparison between experimental [20] and calculated time-temperature profile at a point 12.7 mm away from the centerline on the advancing side. The welding velocity was 0.42 mm/s and the rotational speed was 450 rpm.

gressively increases with x -distance, which is also consistent with the strain rate variations shown in the Fig. 9. An important consequence of the computed viscosity profiles is that high viscosity values beyond a certain critical high value results in lack of plastic flow and define the geometry of the TMAZ.

Fig. 12a and b show the variation of u - and v -components of velocity at different elevations, i.e. z values. It is observed that the variation and magnitude of u - and v -velocities are similar. It is also observed that the peak value of velocity attained at the tool surface is of the order of 50 mm/s. Though the value of ωr is highest at the shoulder periphery, since slip increases as we move away from the

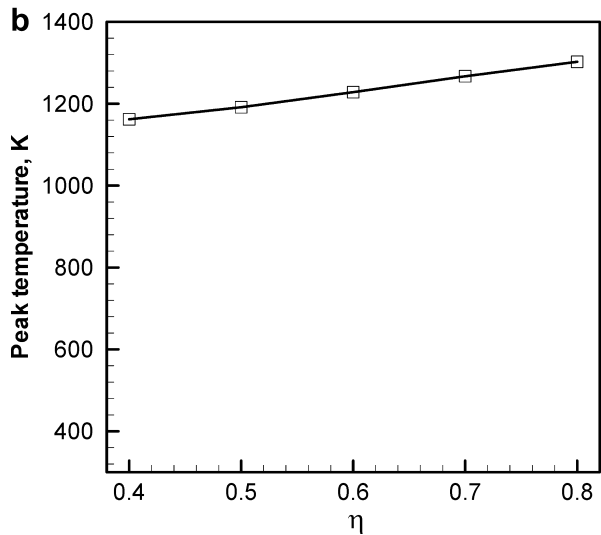
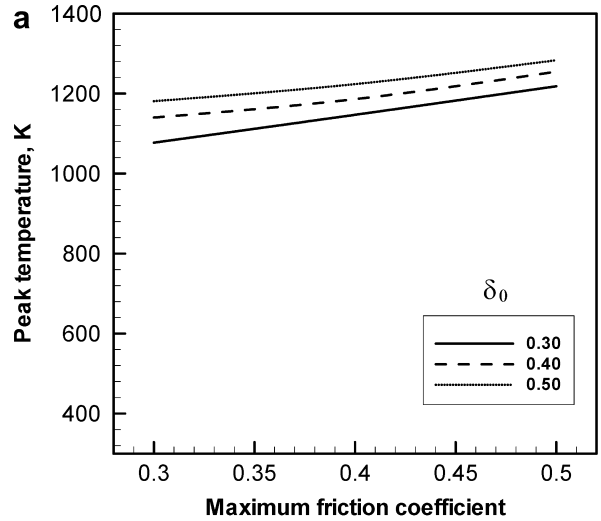


Fig. 9. Variation of peak temperature with (a) friction coefficient and (b) mechanical efficiency factor. The welding velocity was 0.42 mm/s and the rotational speed was 450 rpm.

tool axis, the velocity transmitted to the plasticized work-piece material is not the highest at the periphery.

The viscosity contours at different horizontal planes, i.e. z values, are shown in Fig. 13. The velocity vectors are also plotted in this figure, superimposed on the viscosity contours. It is observed that the viscosity values in the plastic flow region lie in the range of 1×10^5 – 9.9×10^6 Pa s. The maximum viscosity beyond which no significant material flow can be observed is 9.9×10^6 Pa s. The order of magnitude of non-Newtonian viscosity is consistent with the values usually observed in typical viscoplastic processing of materials such as extrusion [41]. The velocity decreases away from the tool pin surface and viscosity increases significantly along that direction. No significant flow occurs when the viscosity is very high. The region of plastic flow decreases with depth.

Temperature contours and velocity vectors on various horizontal planes are depicted in Fig. 14. An interesting

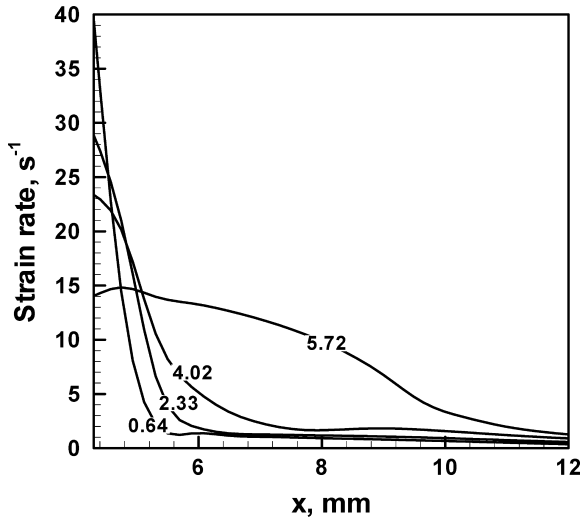


Fig. 10. Strain rate decreases along the weld centerline, away from the tool pin surface opposite to the welding direction at different horizontal planes, at $z = 0.64, 2.33, 4.02$ and 5.72 mm for a 6.35 mm thick plate.

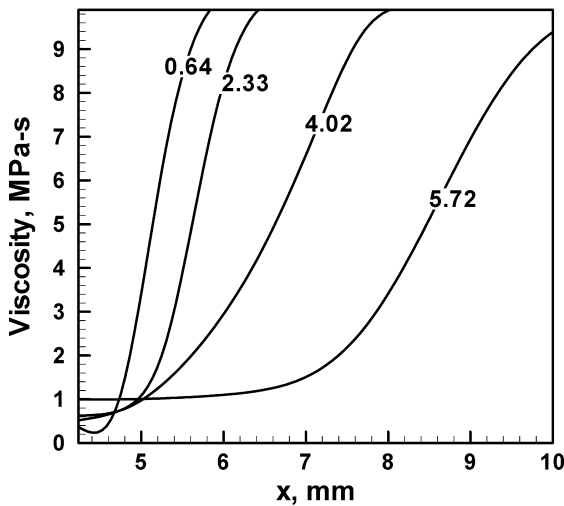


Fig. 11. Variation of viscosity as a function of distance from the tool pin surface opposite to the welding direction at planes corresponding to $z = 0.64, 2.33, 4.02$ and 5.72 mm.

feature to note here is that the area that contains the high plastic flow decreases with distance from the workpiece top surface. The effect of the tool shoulder as a source of momentum is most pronounced in the upper half of the workpiece. The reduction in the area where the flow occurs with distance from the shoulder produces the characteristic shape of the TMAZ.

Fig. 15 shows the stream trace on horizontal planes around the tool pin at three different elevations. The streamlines show the presence of nearly circular, closed streamlines, which indicate recirculating flow of a plug of material around the tool pin. These streamlines are consistent with the presence of a layer of plasticized recirculating metal near the pin surface, and occupy larger areas at higher elevations due to the greater momentum of trans-

port from the rotating shoulder. Beyond the region of recirculating plastic flow, the streamlines indicate that material transfer occurs mainly on the retreating side. Seidel et al. [9] also predicted similar behavior based on a two-dimensional flow model ignoring the effect of the shoulder. Fig. 15 also shows a flow reversal in the advancing side close to the pin, leading to a relatively stagnant zone, which forms closer to the pin at lower elevations. An important consequence of the lack of adequate material flow on the advancing side has been related to the formation of “wormhole” defects by Seidel et al. [9].

The relative rates of heat transfer by convection and conduction is determined by the Peclet number, Pe , given by

$$Pe = \frac{\rho U_c C_p L_c}{k} \quad (23)$$

where U_c is the characteristic velocity and L_c is the characteristic length. This length may be taken as the average thickness of the TMAZ, which may be approximated as

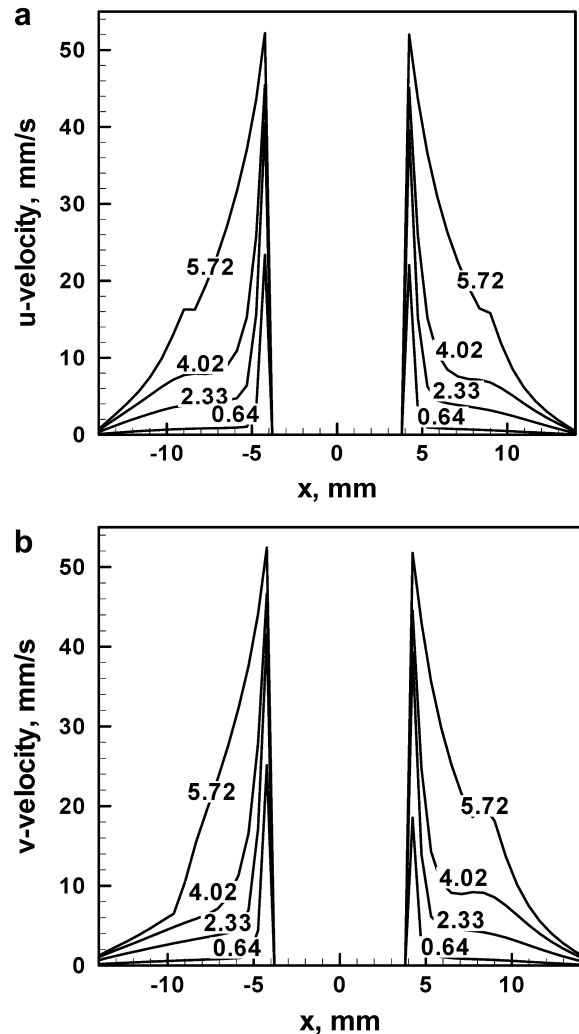


Fig. 12. Plot of variation of (a) x -direction velocity and (b) y -direction velocity as a function of distance from tool surface at planes corresponding to $z = 0.64, 2.33, 4.02$ and 5.72 mm planes.

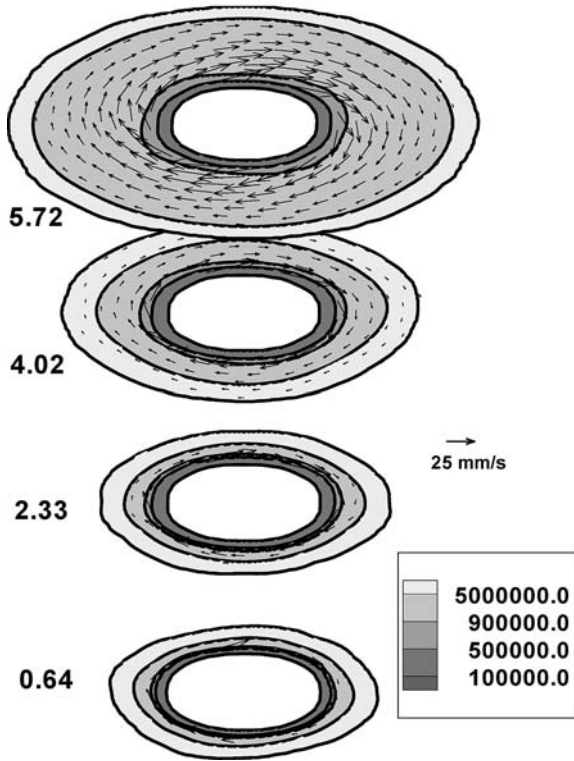


Fig. 13. Plot of spatial variation of viscosity (in Pa s) at $z = 5.72, 4.02, 2.33$ and 0.64 mm planes. Outer-most viscosity contour corresponding to 9.9×10^6 Pa s can be considered the boundary of the plastic flow region and encloses the velocity vectors. The welding velocity was 0.42 mm/s and the rotational speed was 450 rpm.

the distance between the tool pin surfaces to the shoulder periphery. Taking a characteristic length of 3 mm and a characteristic velocity of 25 mm/s from Fig. 12, the value of Peclet number is about 5.5 , which indicates that convec-

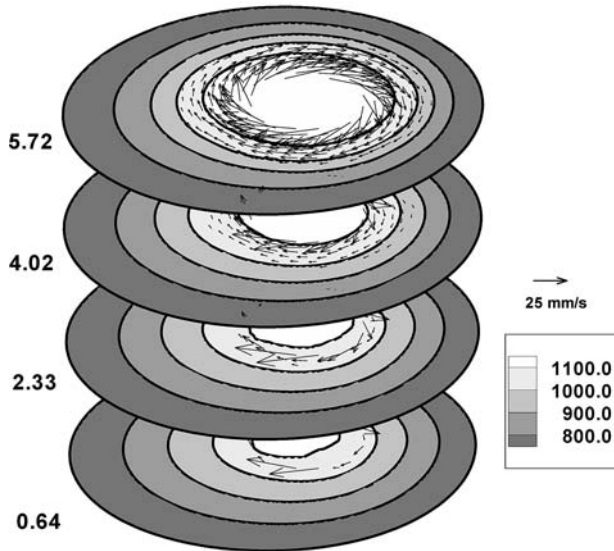


Fig. 14. Plot of temperature contours (in K) and velocity vectors at $z = 5.72, 4.02, 2.33$ and 0.64 mm planes. The welding velocity was 0.42 mm/s and the rotational speed was 450 rpm.

tion is very important for heat transfer during FSW of steel in the high temperature region where significant plastic flow occurs.

4.4. Calculation of torque on the tool

Torque on the tool can be readily measured during a FSW experiment. The torque on the tool was calculated from the numerical model. Torque, T , is based on the shear stress at the surfaces of the tool in contact with the workpiece and is given by

$$T = \oint_A \vec{r}_A \times (\vec{\tau}_t dA) \tag{24}$$

where $\vec{\tau}_t$ is the shear stress and \vec{r}_A is the distance of differential area dA from the tool axis. The summation is done for the three different interfaces of workpiece with tool's shoulder, vertical and horizontal surfaces. The magnitude of shear stress is given by

$$\tau_t = [(1 - \delta)\tau + \delta\mu_t P_N] \tag{25}$$

where P_N denotes the normal pressure, and is equal to P_H at horizontal interfaces and equal to P_V at the vertical interface.

Torque calculated based on Eq. (24) and simulated temperature distribution on the tool surface was 56.7 N m. For the identical welding conditions, the experimentally measured average value of torque was reported to be 55 N m [20] (see Table 3). The good agreement between experimental results and model predictions gives us confidence in the shear stress, friction coefficient and the slip values used in the model.

5. Summary and conclusions

Three-dimensional temperature and plastic flow fields during FSW of mild steel have been calculated by solving the equations of conservation of mass, momentum and energy. The spatially variable non-Newtonian viscosity was determined from the computed values of strain rate, temperature and material properties. Temperature-dependent thermal conductivity, specific heat and yield strength were considered. The computed results show that significant plastic flow occurs near the tool, where convective heat transfer is the main mechanism of heat transfer. The computed results show slight asymmetry of the temperature profiles around the tool because of the rotational and linear motion of the tool. The maximum strain rate during FSW of mild steel was 40 s⁻¹ and the maximum viscosity, above which no significant material flow occurs, was found to be 9.9×10^6 Pa s. The predicted temperature vs. time plots agreed well with experimental results. The predicted torque value of 56.7 N m was in good agreement with the experimentally determined value of 55 N m. The computed streamlines in the horizontal planes around the tool pin showed the presence of nearly circular closed

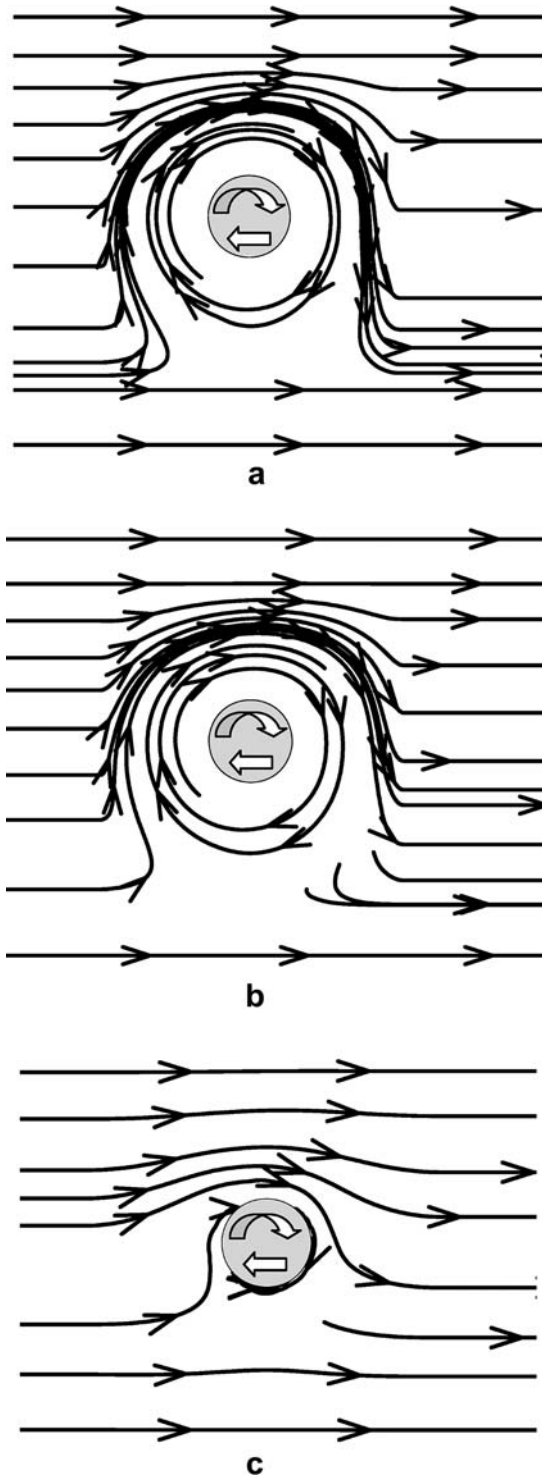


Fig. 15. Streamlines on horizontal planes (a) $z = 5.72$ mm, (b) 4.02 mm and (c) 0.64 mm. The welding velocity was 0.42 mm/s and the rotational speed was 450 rpm.

streamlines, indicating the presence of a plug of material. The region of this recirculating flow expands with elevation because of proximity to the relatively larger rotating shoulder. The streamlines also showed that material flow occurred mainly on the retreating side.

Table 3
Average torque reported in literature for different materials and welding conditions

Reference	Material	Shoulder diameter (mm)	Pin diameter (mm)	Rotational speed (rpm)	Welding speed (mm/s)	Average torque (N m)
[4]	AA2024-T3	18.0	6.0	400	2.0	41.9
[8]	AA6061-T651	25.4	10.0	390	2.36	73.4
[17]	304 stainless steel	19.05	6.35	300	1.693	56.0
[17]	304 stainless steel	19.05	6.35	500	1.693	42.8
[20]	1018 steel	19.0	7.9	528	0.4	55.0

References

- [1] Thomas WM, Nicholas ED, Needham JC, Church MG, Templesmith P., Dawes C. Intl. Patent Application no PCT/GB92/02203 and GB Patent Application no. 9125978.9, 1991.
- [2] Russel MJ, Shercliff HR. Proceedings of the seventh international conference on 'Joints in Aluminum' (INALCO '98), vol. 2. Cambridge: The Welding Institute; 1998. pp.185–95.
- [3] Gould JE, Feng Z. J Mater Process Manuf Sci 1998;7:185–94.
- [4] Schmidt H, Hattel J, Wert J. Model Simul Mater Sci Eng 2004;12:143–57.
- [5] Frigaard Ø, Grong Ø, Midling OT. Metall Mater Trans A 2001;32:1189–200.
- [6] Chao YJ, Qi X, Tang W. Trans ASME 2003;125:138–45.
- [7] Song M, Kovacevic R. Proc Instn Mech Engrs Part B: J Eng Manuf 2004;218:17–33.
- [8] Khandkar MZH, Khan JA, Reynolds AP. Sci Technol Weld Join 2003;8(3):165–74.
- [9] Seidel TU, Reynolds AP. Sci Technol Weld Join 2003;8:175–83.
- [10] Colegrove PA, Shercliff HR. Sci Technol Weld Join 2004;9(4): 345–51.
- [11] Colegrove PA, Shercliff HR. Sci Technol Weld Join 2004;9(4): 352–61.
- [12] Colegrove PA, Shercliff HR. J Mater Process Technol 2005;169(2): 320–7.
- [13] Smith CB, Bendzsak GB, North TH, Hinrichs JF, Noruk JS, Heideman RJ. Proceedings of the ninth international conference on computer technology in Welding, Detroit, MI, 2000, pp. 475–86.
- [14] Ulysse P. Int J Mach Tools Manuf 2002;42:1549–57.
- [15] Nandan R, Roy GG, DebRoy T. Metal Mater Trans A 2006;37(4):1247–59.
- [16] Nandan R, Roy GG, Lienert T, DebRoy T. Sci Technol Weld Join 2006;11(5):526–37.
- [17] Zhu XK, Chao YJ. J Mater Process Technol 2004;146:263–72.
- [18] Cho JH, Boyce DE, Dawson PR. Mater Sci Eng A 2005;398:146–63.
- [19] Hart E. J Eng Mater Technol 1976;98:193–202.
- [20] Lienert TJ, Stellwag Jr WL, Grimmett BB, Warke RW. Weld J 2003;82(1):1s–9s.
- [21] Song M, Kovacevic R. Proc Inst Mech Engrss Part B: J Eng Manuf 2003;217(1):73–85.
- [22] Zhang W, Roy GG, Elmer JW, DebRoy T. J Appl Phys 2003;93: 3022–33.
- [23] Sheppard T, Wright DS. Met Technol 1979;6:215–23.
- [24] Kozlowski PF, Thomas BG, Azzi JA, Wang H. Metall Trans A 1992;23(3):903–18.
- [25] Zienkiewicz OC, Cormeau IC. Int J Numer Methods Eng 1974;8:821–45.
- [26] Brandes EA, Brook GB. Smithells metals reference book. 7th ed. Oxford: Butterworth-Heinemann; 1999.
- [27] Ayer R, Jin HW, Mueller RR, Ling S, Ford S. Scripta Mater 2005;53: 1383–7.
- [28] Carslaw HS, Jaeger JC. Conduction of heat in solids. 2nd ed. Oxford: Clarendon Press; 1959. pp. 87–9.
- [29] Bastier A, Maitournam MH, Dang Van K, Roger F. Sci Technol Weld Join 2006;11(3):278–88.
- [30] Patankar SV. Numerical heat transfer and fluid flow. New York: Hemisphere Publishing Corporation; 1980.
- [31] De A, DebRoy T. Welding J 2005;84(7):101–12.
- [32] Mishra S, DebRoy T. J Phys D 2005;38:2977–85.
- [33] Zhang W, DebRoy T, Elmer JW. Sci Technol Weld Join 2005;10(5): 574–82.
- [34] Zhang W, DebRoy T, Palmer TA, Elmer JW. Acta Mater 2005; 53(16):4441–53.
- [35] Mishra S, DebRoy T. J Appl Phys 2005;98:044902.
- [36] He X, DebRoy T, Fuerschbach PW. J Appl Phys 2004;96:4547–55.
- [37] Mundra K, DebRoy T, Kelkar KM. Numer Heat Transfer 1996;29: 115.
- [38] Deng Z, Lovell MR, Tagavi KA. J Manuf Sci Eng 2001;123:647–53.
- [39] Kong HS, Ashby MF. MRS Bulletin 1991(October).
- [40] Vill VI. Friction welding of metals. New York: AWS/Reinhold; 1962. pp. 42–51.
- [41] Halley PJ, Mackay ME. J Rheol 1994;38(1):41–51.